Development and validation of a short-lag spatial coherence theory for photoacoustic imaging

Michelle T. Graham[1] and Muyinatu A. Lediju Bell[1,2]

[1]Department of Electrical and Computer Engineering, Johns Hopkins University, Baltimore, MD, United States
[2]Department of Biomedical Engineering, Johns Hopkins University, Baltimore, MD, United States

ABSTRACT

We previously derived a theoretical expression for spatial coherence in photoacoustic data and utilized it to study properties of the short-lag spatial coherence (SLSC) beamformer applied to photoacoustic imaging. In this paper, an updated version of our theoretical equation is evaluated to generate SLSC images of a point target, a 1.2 mm diameter target, and corresponding lateral profiles through the target centers. We compared SLSC images simulated solely based on our theory to SLSC images created after beamforming acoustic channel data from k-Wave simulations of a 1.2 mm-diameter disc target. This process was repeated for a point target and the full width at half of the maximum signal amplitude in each point target image was measured to estimate the resolution of each simulated imaging system. Resolution was measured as a function of lag (i.e., transducer element spacing), and excellent agreement was obtained in the short-lag region corresponding to 3-11% of the receive aperture. Beyond this region, resolution measurements diverged by a maximum of 1 mm between the two types of simulated images. These results indicate the potential for both simulation methods to be utilized as independent resources to study coherence-based photoacoustic beamformers.

Keywords: coherence beamformers, k-Wave, simulation

1. INTRODUCTION

Short-lag spatial coherence (SLSC) beamforming displays coherence values to form images, rather than relying on the amplitude-based measurements of the more standard delay-and-sum (DAS) and Fourier-based beamforming and photoacoustic image reconstruction techniques.[1,2] SLSC beamforming was initially developed for ultrasound imaging, demonstrating considerable improvements in contrast, contrast-to-noise ratio, and signal-to-noise ratio, when compared to traditional amplitude-based ultrasound images of *in vivo* hearts,[3] livers,[4] and fetuses,[5] particularly in high-noise environments that otherwise produce ultrasound images with significant acoustic clutter. In addition, the resolution of point-like targets demonstrated significant improvements in these high-noise environments.[6]

The SLSC technique was later applied to experimental photoacoustic images with similar improvements. In photoacoustic imaging, pulsed laser light is transmitted, and the rapid thermal expansion and contraction of light-absorbing targets emits an acoustic wave that is received by an ultrasound transducer.[7] Blood and metal are typical photoacoustic targets,[7–9] because their optical absorption properties are orders of magnitude larger than that of surrounding biological tissues. SLSC is beneficial for visualizing these photoacoustic targets in scenarios with insufficient laser fluence, which occurs when imaging deep structures like prostate brachytherapy seeds[10] or when using low-energy pulsed laser diodes.[11,12] We recently derived theory to describe the SLSC beamforming process when applied to photoacoustic images in order to understand the full breadth of potential applications and enable the optimization of photoacoustic SLSC image display.[13] While this theory accurately identified the presence of a photoacoustic target, line plots through the resulting SLSC images of these images showed some oscillations in the background region surrounding the target, and these oscillations were not present in corresponding experimental data.[13]

E-mail: mgraha33@jhu.edu

The work in this paper makes one update to our theoretical derivation, and this update removes the background oscillations previously observed. We then directly compare SLSC images simulated based on this updated theory to SLSC images created after beamforming acoustic data generated by k-Wave simulation software[14].

2. PHOTOACOUSTIC SPATIAL COHERENCE THEORY

A summary of our derivation for photoacoustic spatial coherence appears in our previous conference paper,[13] which states that the equation for photoacoustic spatial covariance, R_p, is given by:

$$R_p(\mathfrak{m}, x, x_k, z, \lambda) = e^{-(j2\pi x_k \mathfrak{m})/\lambda z} \cdot z^{-2} \int_{-\infty}^{\infty} \mid \chi(f)\Gamma(x)\mu_a(x)F(z,\mu_a) \mid^2 e^{-(j2\pi x \mathfrak{m})/\lambda z} dx \tag{1}$$

where $\mathfrak{m}$ is the lag (i.e., spatial distance between any two elements on a transducer), x is the axis coinciding with the lateral dimension of the transducer with its origin located at the center of the transducer, x_k is the lateral position of one A-line in the final image, z is the axis that corresponds to the axial dimension of the transducer (i.e., depth dimension) with its origin located at the surface of the transducer, λ is the acoustic wavelength, f is the acoustic frequency (which is related to λ through the speed of sound in the medium), $\chi(f)$ is the random distribution of spatially incoherent absorbers as a function of f, $\Gamma(x)$ is the Grüneisen parameter as a function of x, $\mu_a(x)$ is the optical absorption coefficient as a function of x, and $F(z, \mu_a)$ is the fluence which varies as a function of z and μ_a. Note that Eq. (1) is the scaled Fourier transform of the square of χ multiplied by the initial pressure distribution at the absorber surface, which is defined by the product of Γ, μ_a, and F. The spatial frequency in this Fourier transform is given by $u = \mathfrak{m}/\lambda z$. This Fourier transform is then multiplied by a phase term that depends of the lateral position of the line being imaged (i.e., x_k), which was introduced by the shifting property of the Fourier transform.

In order to form an SLSC image, Eq. (1) is first evaluated at spatial frequencies, $u = \mathfrak{m}/\lambda z$, then averaged over multiple wavelengths, λ, based on the assumption that the spatial coherence observed by an aperture is the average of the spatial coherence curves obtained at the multiple acoustic frequencies within the bandwidth of an ultrasound probe. The step that averages over multiple wavelengths was not included in our original derivation, and inclusion of this update removes the oscillations previously observed in the background of simulated SLSC line profiles.[13] After averaging over multiple wavelengths, the resulting coherence curves are summed up to a specific lag value, M, to form each pixel in the simulated SLSC image, yielding our new imaging equation:

$$SLSC_{pixel}(x_k, z) = \frac{1}{\lambda_U - \lambda_L} \int_0^M \int_{\lambda_L}^{\lambda_U} R_p(\mathfrak{m}, x, x_k, z, \lambda) d\lambda d\mathfrak{m} \tag{2}$$

where λ_U and λ_L are the upper and lower limits, respectively, of the acoustic wavelengths corresponding to the -6dB frequency limits of the ultrasound probe bandwidth. In summary, to obtain a simulated SLSC image using our updated theory, a coherence curve is first generated using Eq. (1) and subsequently integrated using Eq. (2) for each pixel in the SLSC image.

3. METHODS

3.1 Theoretical Simulations

Eq. (1) was evaluated at spatial frequencies $u = \mathfrak{m}/\lambda z$, using realistic transducer parameters and phantom properties to obtain spatial coherence curves. A receiving ultrasound transducer with 128 elements, 0.3 mm pitch, 3.84 cm total length, and 3 MHz to 7.25 MHz bandwidth was modeled. Theoretical SLSC pixel values were obtained by averaging over acoustic wavelengths within the bandwidth of the ultrasound transducer (i.e., $\lambda_L = 212\ \mu m$ to $\lambda_U = 513\ \mu m$) and summing the resulting coherence curves up to a specific lag value, M, as described by Eq. (2). The simulated phantom consisted of a circular region (representing either a point target or a 1.2 mm-diameter target) of high optical absorption, surrounded by a region of low optical absorption, as illustrated in Fig. 1. The simulated fluence profile was a uniform light sheet illuminating the entire field of view of the transducer.

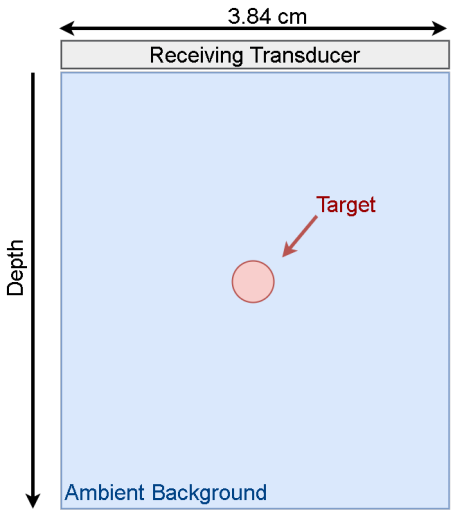

Figure 1. Schematic diagram of the simulated phantom and transducer for both theoretical and k-Wave simulations. In both simulation sets, the target size was varied from a point target to a 1.2 mm diameter target. The aperture differed in number of elements and pitch (128 elements with 0.3 mm pitch and 384 elements with 0.1 m pitch for theory and k-Wave, respectively) between the two simulations, but had the same total width of 3.84 cm and therefore same field of view.

3.2 k-Wave Simulations

Photoacoustic simulations were performed in k-Wave for a point target and 1.2 mm diameter target. The modeled transducer contained 384 elements, 0 mm kerf, and 0.1 mm pitch, resulting in a transducer of equal length to the receiving transducer described in Section 3.1 and shown in Fig. 1. The 2D k-Wave channel data was bandpass filtered to model the band-limiting effects of a 3 MHz to 7.25 MHz ultrasound transducer and to match the acoustic frequency response of the theoretical simulated data. SLSC images were generated by beamforming the channel data generated by k-Wave, as described in previous publications when creating experimental SLSC images.[10–12]

4. RESULTS

SLSC images formed with theoretical and k-Wave simulations of a 1.2 mm target are shown in Figs. 2(a) and 2(b), respectively. Due to the differences in pitch between the two simulation sets, both images are displayed at 11% of the aperture, rather than with the same absolute lag value. The corresponding line plots through

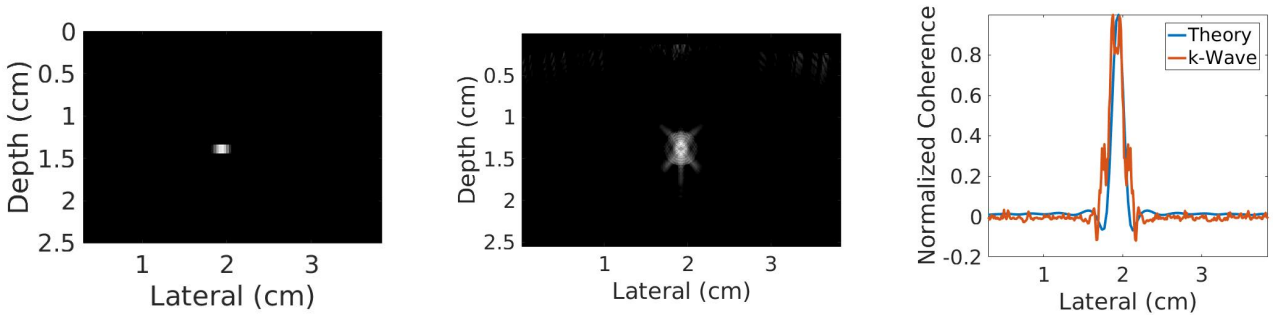

(a) (b) (c)

Figure 2. (a) Theoretical and (b) k-Wave photoacoustic SLSC images of a 1.2 mm diameter target displayed with a lag that is equivalent to 11% of the ultrasound transducer aperture. Images are normalized and thresholded by a minimum of 0.1. (c) Corresponding lateral line plots through the center of each target show similar full-width-at-half-maximum (FWHM) measurements.

these images are shown in Fig. 2(c). Qualitatively, the resolution of the two images appear similar, based on the normalized line plots shown in Fig. 2(c). However, in the k-Wave image, the region above and below the target contains artifacts that are not present in the theoretical simulation. These artifacts decrease image clarity and target localization. We also observe a decrease in coherence at the center of the target in the k-Wave simulation image that is not present in theoretical image. These discrepancy is also evident at the center of the line plots in Fig. 2(c).

The process used to create the images shown in Fig. 2 was repeated for a point target. These point target data were used to quantify the resolution of each imaging method as a function of lag. We used full-width-at-half-maximum (FWHM) measurements as an estimate of resolution. Fig. 3(a) shows that the FWHM decays exponentially with increasing lag for both data types. The primary difference between the two measurement occurs at higher lag values in the region we refer to as the steady-state FWHM, where the best resolution of each system is achieved. Additional deviations are observed in first few lags.

Specifically, SLSC images created with the k-Wave simulation data initially have lower FWHM measurements at lags corresponding to 0-3% of the aperture (e.g., 4.9 mm at 1%) and reach a lower steady-state FWHM (0.2 mm) at lags greater than 25% of the aperture. In contrast, images created based on the theoretical derivation initially have higher FWHM measurements at lags corresponding to 0-3% of the aperture (e.g., 7.6 mm at 1%) and reach a higher steady-state FWHM of 1.2 mm at lags greater than 11% of the aperture. Otherwise, the two simulation methods have excellent agreement in the short-lag range corresponding to 3-11% of the aperture. An example of the SLSC line plots obtained with a lag value equivalent to 11% of the aperture for point targets created with the two simulation methods is shown in Fig. 3(b).

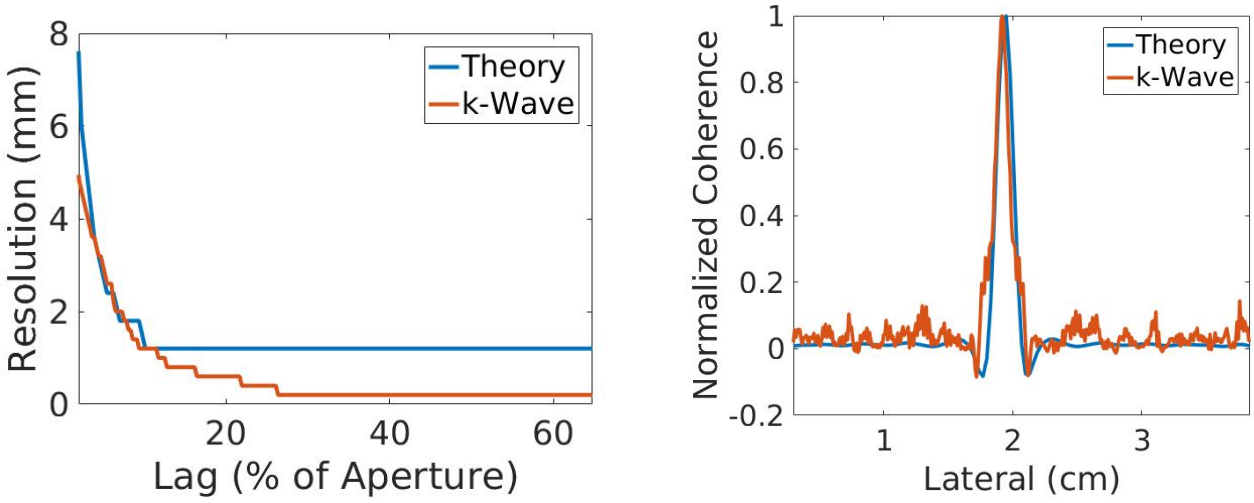

(a) (b)

Figure 3. (a) FWHM as a function of lag (displayed a percentage of the total aperture) shows comparable resolution up to a lag that is equivalent to 11% of the ultrasound transducer aperture, after which resolution measurements diverge by a maximum of 1 mm between the two simulation sets. (b) Lateral SLSC line plots of the point target created with theoretical and k-Wave simulations are displayed with a lag that is equivalent to 11% of the ultrasound transducer aperture.

5. DISCUSSION AND CONCLUSIONS

This work is the first to compare theoretical simulations of photoacoustic spatial coherence to SLSC data generated from k-Wave simulations. Qualitative and quantitative analyses of a point target and a 1.2 mm diameter target reveal similarities and differences when imaging with the two simulation methods. Excellent lateral resolution agreement was obtained in the short-lag region corresponding to 3-11% of the receive aperture. These results provide initial insights into the capabilities of both simulation methods to be utilized as independent

resources when studying coherence-based photoacoustic beamformers. However, there are discrepancies in coherence amplitude at the target center. Therefore, future work will compare both simulation methods with experimental data.

REFERENCES

[1] Lediju, M. A., Trahey, G. E., Byram, B. C., and Dhal, J. J., "Short-lag spatial coherence of backscattered echose: Imaging characteristics," *IEEE Transactions on Ultrasonics, Ferroelectrics, and Frequency Control* (2011).

[2] Lediju Bell, M., Song, D., and Boctor, E., "Coherence-based photoacoustic imaging of brachytherapy seeds implanted in a canine prostate," *Proceedings of SPIE* **9040** (2014).

[3] Bell, M. A. L., Goswami, R., Kisslo, J. A., Dahl, J. J., and Trahey, G. E., "Short-lag spatial coherence imaging of cardiac ultrasound data: Initial clinical results," *Ultrasound in medicine & biology* **39**(10), 1861–1874 (2013).

[4] Jakovljevic, M., Trahey, G. E., Nelson, R. C., and Dahl, J. J., "In vivo application of short-lag spatial coherence imaging in human liver," *Ultrasound in medicine & biology* **39**(3), 534–542 (2013).

[5] Kakkad, V., Dahl, J., Ellestad, S., and Trahey, G., "In vivo application of short-lag spatial coherence and harmonic spatial coherence imaging in fetal ultrasound," *Ultrasonic imaging* **37**(2), 101–116 (2015).

[6] Lediju Bell, M., Dahl, J., and Trahey, G., "Resolution and brightness characteristics of short-lag spatial coherence (SLSC) images," *IEEE Transactions on Ultrasonics, Ferroelectrics, and Frequency Control* **62**(7), 1265–1276 (2015).

[7] Beard, P., "Biomedical photoacoustics," *Interface Focus* **1**(4) (2011).

[8] Bouchard, R., Sahin, O., and Emelianov, S., "Ultrasound-guided photoacoustic imaging: current state and future development," *IEEE transactions on ultrasonics, ferroelectrics, and frequency control* **61**(3), 450–466 (2014).

[9] Su, J. L., Bouchard, R. R., Karpiouk, A. B., Hazle, J. D., and Emelianov, S. Y., "Photoacoustic imaging of prostate brachytherapy seeds," *Biomedical optics express* **2**(8), 2243–2254 (2011).

[10] Bell, M. A. L., Kuo, N., Song, D. Y., and Boctor, E. M., "Short-lag spatial coherence beamforming of photoacoustic images for enhanced visualization of prostate brachytherapy seeds," *Biomedical Optics Express* (2013).

[11] Bell, M. A. L., Guo, X., Kang, H. J., and Boctor, E. M., "Improved contrast in laser-diode-based photoacoustic images with short-lag spatial coherence beamforming," *2014 IEEE International Ultrasonics Symposium* (2014).

[12] Gandhi, N., Allard, M., Kim, S., Kazanzides, P., and Lediju Bell, M., "Photoacoustic-based approach to surgical guidance performed with and without a da vinci robot," *Journal of Biomedical Optics* **22**(12) (2017).

[13] Graham, M. T. and Bell, M. A. L., "Theoretical application of short-lag spatial coherence to photoacoustic imaging," *Proceedings of the 2017 IEEE International Ultrasonics Symposium* (2017).

[14] Treeby, B. E. and Cox, B. T., "k-Wave: MATLAB toolbox for the simulation and reconstruction of photoacoustic wave-fields," *J. Biomed. Opt.* **15**(2), 021314 (2010).